Dalton Transactions

PAPER

View Article Online
View Journal | View Issue

Cite this: *Dalton Trans.*, 2015, **44**, 19163

Synthesis, crystal structure, optical and thermal properties of lanthanide hydrogen-polyphosphates Ln[H(PO$_3$)$_4$] (Ln = Tb, Dy, Ho)†

Katharina Förg and Henning A. Höppe*

Received 13th July 2015,
Accepted 7th October 2015

DOI: 10.1039/c5dt02648b

www.rsc.org/dalton

Lanthanide hydrogen-polyphosphates Ln[H(PO$_3$)$_4$] (Ln = Tb, Dy, Ho) were synthesised as colourless (Ln = Tb, Dy) and light pink (Ln = Ho) crystalline powders by reaction of Tb_4O_7/Dy_2O_3/Ho_2O_3 with H_3PO_3 at 380 °C. All compounds crystallise isotypically ($P2_1/c$ (no. 14), Z = 4, a_{Tb} = 1368.24(4) pm, b_{Tb} = 710.42(2) pm, c_{Tb} = 965.79(3) pm, β_{Tb} = 101.200(1)°, 3112 data, 160 parameters, wR_2 = 0.062, a_{Ho} = 1363.34(5) pm, b_{Ho} = 709.24(3) pm, c_{Ho} = 959.07(4) pm, β_{Ho} = 101.055(1)°, 1607 data, 158 parameters, wR_2 = 0.058). The crystal structure comprises two different infinite helical chains of corner-sharing phosphate tetrahedra. In-between these chains the lanthanide ions are located, coordinated by seven oxygen atoms belonging to four different polyphosphate chains. Vibrational, UV/Vis and fluorescence spectra of Ln[H(PO$_3$)$_4$] (Ln = Tb, Dy, Ho) as well as Dy[H(PO$_3$)$_4$]:Ln (Ln = Ce, Eu) and the magnetic and thermal behaviour of Tb[H(PO$_3$)$_4$] are reported.

1 Introduction

In general, phosphates exhibit a large variety of structures and composition. Besides monophosphates, various condensed oligo-, long-chain polyphosphates and cyclophosphates exist.[1,2] Phosphates doped with lanthanides or stoichiometric lanthanide phosphates, such as $Sr_3(PO_4)_5Cl$:Eu^{3+}/Eu^{2+}, $LaPO_4$:Ce^{3+},Tb^{3+}, (Y,Gd)PO_4:Eu^{3+},[3–7] Ln$(PO_3)_3$:Eu^{3+} (Ln = Y, Gd, Lu),[8] α-Sr$(PO_3)_2$:Eu^{2+},Mn^{2+}, Sr$M(P_2O_7)$:Eu^{2+},Mn^{2+} (M = Zn, Sr)[9,10] and BaCa$(PO_3)_4$:Eu^{2+} (ref. 11), reveal great potential for optical applications as luminescent materials. Many transitions between the energy levels of the Ln^{3+} ions are in the visible range (12500–25000 cm^{-1}).[12,13] Due to the strong shielding of the 5s and 5p orbitals, crystal field splitting is very small, and weak 4f–4f transitions occur, leading to the characteristic line emissions.[4,7,14] Since these are parity forbidden, they only become allowed by an admixture of states of the opposite parity.[12,13] Despite the rather low emission, a good colour rendering can be achieved.[4,7]

Acid polyphosphates with the sum formula Ln[H(PO$_3$)$_4$] (Ln = Sm, Eu) are known to crystallise isostructurally to Bi[H(PO$_3$)$_4$][15] in the triclinic space group $P\bar{1}$.[16] Surprisingly, acid polyphosphates of the elements at the origin of the lanthanide row (La, Pr, Nd) and at the end (Tm, Yb) have not yet been observed. Instead, only non-protonated polyphosphates and ultraphosphates are formed depending on the synthesis temperature.[17] Ln[H(PO$_3$)$_4$] (Ln = Tb–Er) crystallises in the monoclinic space group $P2_1/c$. Gd[H(PO$_3$)$_4$] represents an exception, which crystallises in both configurations at the same time. Up to now only the crystal structure of Er[H(PO$_3$)$_4$] was solved from single-crystal data.[17] With regard to optical applications, both the spectroscopic properties and the thermal stability of the host lattice are important characteristics.

Herein we study the crystal structures of Ln[H(PO$_3$)$_4$] (Ln = Tb, Dy, Ho) determined from single-crystal data (Ln = Tb, Ho) and refined *via* a Rietveld refinement (Ln = Dy) as well as their optical, magnetic and thermal properties.

Table 1 MAPLE calculations for Ln[H(PO$_3$)$_4$] (Ln = Tb, Ho)

Tb[H(PO$_3$)$_4$]	α-TbP_3O_9 [22] + 0.5H_2O [34] + 0.5P_2O_5 [35]
MAPLE = 98 590 kJ mol^{-1} (Δ = 0.1%)	MAPLE = 98 466 kJ mol^{-1}
Ho[H(PO$_3$)$_4$]	α-HoP_3O_9 [22] + 0.5H_2O [34] + 0.5P_2O_5 [35]
MAPLE = 98 811 kJ mol^{-1} (Δ = 0.5%)	MAPLE = 98 326 kJ mol^{-1}

Institut für Physik, Universität Augsburg, Universitätsstraße 1, Augsburg, Germany. E-mail: henning@ak-hoeppe.de; Fax: +49 821-598-5955

†Electronic supplementary information (ESI) available. See DOI: 10.1039/c5dt02648b

Table 2 Absorption band energies for the strongest transitions in $Tb[H(PO_3)_4]$ and in free Tb^{3+} ions between 225 and 800 nm

No.	Absorption	λ/nm	$Tb[H(PO_3)_4]$ energy/10^3 cm^{-1}	Free Tb^{3+} (ref. 42) energy/10^3 cm^{-1}
1	$^7F_6 \rightarrow {}^5H_7$	319	31.3	31.6
2	$^7F_6 \rightarrow {}^5G_2$	336	29.8	29.6
3	$^7F_6 \rightarrow {}^5L_9$	351	28.5	28.5
4	$^7F_6 \rightarrow {}^5G_5$	358	27.9	27.8
5	$^7F_6 \rightarrow {}^5L_{10}$	369	27.1	27.1
6	$^7F_6 \rightarrow {}^5G_6$	377	26.5	26.4
7	$^7F_6 \rightarrow {}^5D_4$	486	20.6	20.5

Table 3 Absorption band energies for the strongest transitions in $Dy[H(PO_3)_4]$ and in free Dy^{3+} ions between 225 and 800 nm

No.	Absorption	λ/nm	$Dy[H(PO_3)_4]$ energy/10^3 cm^{-1}	Free Dy^{3+} (ref. 42) energy/10^3 cm^{-1}
1	$^6H_{15/2} \rightarrow {}^4D_{7/2}$	295	33.9	33.8
2	$^6H_{15/2} \rightarrow {}^6P_{3/2}$	325	30.8	30.8
3	$^6H_{15/2} \rightarrow {}^4F_{5/2} + {}^4D_{5/2}$	338	29.6	29.6
4	$^6H_{15/2} \rightarrow {}^6P_{7/2}$	350	28.6	28.6
5	$^6H_{15/2} \rightarrow {}^6P_{5/2}$	364	27.5	27.5
6	$^6H_{15/2} \rightarrow {}^4K_{17/2}$	378	26.5	26.4
7	$^6H_{15/2} \rightarrow {}^4I_{13/2}$	386	25.9	25.9
8	$^6H_{15/2} \rightarrow {}^4G_{11/2}$	425	23.5	23.3
9	$^6H_{15/2} \rightarrow {}^4I_{15/2}$	452	22.1	22.3
10	$^6H_{15/2} \rightarrow {}^4F_{9/2}$	473	21.1	21.1
11	$^6H_{15/2} \rightarrow {}^6F_{3/2}$	753	13.3	13.2

Table 4 Absorption band energies for the strongest transitions in $Ho[H(PO_3)_4]$ and in free Ho^{3+} ions between 225 and 800 nm

No.	Absorption	λ/nm	$Ho[H(PO_3)_4]$ energy/10^3 cm^{-1}	Free Ho^{3+} (ref. 41) energy/10^3 cm^{-1}
1	$^5I_8 \rightarrow {}^3H_6 + {}^1I_6$	219	45.7	45.7
2	$^5I_8 \rightarrow {}^3F_4 + {}^5D_4$	241	41.6	41.5
3	$^5I_8 \rightarrow {}^5D_3$	250	40.0	40.0
4	$^5I_8 \rightarrow {}^3I_7$	261	38.2	38.5
5	$^5I_8 \rightarrow {}^3P_0$	278	36.0	36.0
6	$^5I_8 \rightarrow {}^5G_4 + {}^5D_4 + {}^3G_4$	290	34.5	34.8
7	$^5I_8 \rightarrow {}^3F_4 + {}^3H_4 + {}^3G_4$	334	29.9	30.0
8	$^5I_8 \rightarrow {}^3L_9$	346	28.9	29.0
9	$^5I_8 \rightarrow {}^3H_6$	361	27.7	27.7
10	$^5I_8 \rightarrow {}^5G_4$	386	25.9	25.8
11	$^5I_8 \rightarrow {}^5G_5 + {}^3G_5$	417	24.0	24.0
12	$^5I_8 \rightarrow {}^5F_1$	451	22.2	22.4
13	$^5I_8 \rightarrow {}^3K_8$	468	21.4	21.3
14	$^5I_8 \rightarrow {}^5F_2$	473	21.1	21.1
15	$^5I_8 \rightarrow {}^5F_3$	485	20.6	20.7
16	$^5I_8 \rightarrow {}^5F_4$	538	18.6	18.6
17	$^5I_8 \rightarrow {}^5F_5$	648	15.4	15.5

2 Crystal structure

$Ln[H(PO_3)_4]$ (Ln = Tb, Dy, Ho) crystallise isotypically to $Er[H(PO_3)_4]$[17] in the centrosymmetric monoclinic space group $P2_1/c$ (no. 14) (Tables 5–9 and 11). The anionic partial structure of $Ln[H(PO_3)_4]$ (Ln = Tb, Dy, Ho) consists of two different infinite helical corner-sharing phosphate chains arranged parallel to each other along [010] with alternating poly-hydrogenphosphate and polyphosphate chains (Fig. 1).

Table 5 Single-crystal data and structure refinements of $Ln[H(PO_3)_4]$ (Ln = Tb, Ho)

	$Tb[H(PO_3)_4]$	$Ho[H(PO_3)_4]$
Temperature/K	293(2)	296(2)
Molar weight/g mol^{-1}	475.81	481.77
Crystal system	Monoclinic	Monoclinic
Space group	$P2_1/c$ (no. 14)	$P2_1/c$ (no. 14)
Crystal shape	Plate	Irregular
Crystal size/mm^3	0.047 × 0.018 × 0.019	0.050 × 0.018 × 0.020
Colour	Colourless	Pink/yellow
a/pm	1368.24(4)	1363.34(5)
b/pm	710.42(2)	709.24(3)
c/pm	965.79(3)	959.07(4)
β/°	101.200(1)	101.055(1)
Volume/10^6 pm^3	920.89(5)	910.15(6)
Z	4	4
Calculated density D_x/g cm^{-3}	3.432	3.499
Absorption coefficient μ/mm^{-1}	8.440	9.462
$F(000)$	888	896
Radiation (λ/Å)	Mo-K$_\alpha$ (0.7093)	Mo-K$_\alpha$ (0.7093)
Diffractometer	Bruker D8 Venture	Bruker D8 Venture
Absorption correction	Multi-scan	Multi-scan
Transmission factor (min./max.)	0.6359/0.7457	0.6029/0.7458
Index range $h\|k\|l$ (min./max.)	0/16|−8/0|−11/11	−16/16|−8/8|−11/11
Theta range/°	3.04 ≤ Θ ≤ 25.00	3.04 ≤ Θ ≤ 25.00
Reflections collected	3112	27195
Independent reflections	3111	1607
Observed reflections ($I > 2\sigma$)	2790	1421
R_{int}	—	0.0537
Refined parameters	160	158
R_1 (all data)	0.028	0.029
wR_2 (all data)	0.062	0.058
Weighting scheme	$w^{-1} = \sigma^2 F_o^2 + (0.0389P)^2$ $P = (F_o^2 + 2F_c^2)/3$	$w^{-1} = \sigma^2 F_o^2 + (0.0423P)^2 + 1.5847P$ $P = (F_o^2 + 2F_c^2)/3$
GooF	1.131	1.030
Residual electron density (min./max.)/e$^-$ Å^{-3}	−0.499/0.144	−0.841/1.981

The protonated chain (A) reveals a larger diameter compared to the non-protonated polyphosphate chain (B) (Fig. 2) due to the widened P–O–P angles (136° in A *vs.* 130–133° in B).

The adjacent A and B chains in the a and c directions, respectively, exhibit a phase shift of 180° towards each other (Fig. 3).

In the phosphate tetrahedra P–O bond lengths range between 146 and 161 pm. The P–O_H bond is 153 pm long. P–O_{br} distances range between 156 and 161 pm, whereas P–O_{term} distances range between 146 and 150 pm. These values correspond very well to the data found for other poly-hydrogenphosphates[15–17] or polyphosphates.[18–23] In general, P–O distances increase from P–O_{term} to P–O_H and up to P–O_{br} due to the decreasing effective negative charge on the involved oxygen atom which leads to weaker electrostatic interactions between P and O. Angles of the P_{OH}–O_{br}–P_O and P_O–O_{br}–P_O bridges range between 135 and 137° and between 129

Table 6 Refined atomic coordinates, Wyckoff symbols and isotropic displacement parameters U_{eq}/Å^2 in Tb[H(PO$_3$)$_4$]

Atom	Wyckoff symbol	x	y	z	U_{eq}
Tb1	4e	0.729401(15)	0.05792(3)	0.05897(2)	0.00704(9)
P1	4e	0.90133(8)	−0.32485(16)	0.12591(13)	0.0083(3)
P2	4e	0.90026(9)	0.15142(17)	−0.18737(12)	0.0080(3)
P3	4e	0.61157(9)	−0.20990(17)	0.29579(12)	0.0077(2)
P4	4e	0.59385(9)	0.40127(16)	0.20937(12)	0.0078(3)
$O_{br}1$	4e	0.9446(3)	−0.4771(5)	0.2377(3)	0.0135(7)
$O_{br}2$	4e	0.9990(2)	−0.2305(4)	0.0948(3)	0.0114(7)
$O_{br}3$	4e	0.5802(2)	−0.3766(4)	0.1876(3)	0.0117(7)
$O_{br}4$	4e	0.5152(2)	−0.1724(4)	0.3594(3)	0.0098(7)
$O_{term}1$	4e	0.8343(3)	−0.1896(5)	0.1741(3)	0.0145(8)
$O_{term}2$	4e	0.8414(3)	0.0764(5)	−0.0888(3)	0.0174(8)
$O_{term}3$	4e	0.8587(3)	0.2914(5)	−0.2952(3)	0.0156(8)
$O_{term}4$	4e	0.6343(3)	−0.0457(4)	0.2130(3)	0.0132(7)
$O_{term}5$	4e	0.6902(3)	−0.2722(4)	0.4168(3)	0.0123(7)
$O_{term}6$	4e	0.6158(2)	0.3586(5)	0.3627(3)	0.0115(7)
$O_{term}7$	4e	0.6615(2)	0.3364(4)	0.1191(3)	0.0114(7)
O_H1	4e	0.8569(3)	−0.4300(5)	−0.0105(4)	0.0158(8)
H1	4e	0.804(3)	−0.350(8)	−0.048(5)	0.05

O_{br} = bridging oxygen atom; O_{term} = terminal oxygen atom; O_H = hydroxyl group.

Table 7 Anisotropic displacement parameters U_{ij}/Å^2 in Tb[H(PO$_3$)$_4$]

Atom	U_{11}	U_{22}	U_{33}	U_{12}	U_{13}	U_{23}
Tb1	0.00640(13)	0.00779(13)	0.00678(13)	−0.00024(9)	0.00093(10)	0.00006(9)
P1	0.0056(6)	0.0087(6)	0.0100(6)	0.0002(5)	0.0001(5)	−0.0004(5)
P2	0.0051(6)	0.0086(6)	0.0104(6)	0.0007(5)	0.0017(5)	0.0010(5)
P3	0.0068(6)	0.0074(6)	0.0082(5)	0.0005(5)	−0.0005(5)	−0.0001(5)
P4	0.0070(6)	0.0062(6)	0.0094(6)	−0.0008(5)	−0.0001(5)	−0.0002(5)
$O_{br}1$	0.0099(18)	0.0108(17)	0.0184(19)	0.0068(14)	−0.0009(14)	0.0002(15)
$O_{br}2$	0.0129(19)	0.0104(17)	0.0091(14)	0.0030(14)	−0.0025(13)	−0.0011(14)
$O_{br}3$	0.0195(19)	0.0051(16)	0.0087(16)	−0.0010(13)	−0.0021(14)	0.0022(15)
$O_{br}4$	0.0076(17)	0.0136(19)	0.0084(16)	0.0024(13)	0.0021(13)	0.0023(14)
$O_{term}1$	0.020(2)	0.0089(18)	0.0137(17)	0.0017(14)	0.0021(15)	0.0029(16)
$O_{term}2$	0.0116(18)	0.027(2)	0.0156(17)	−0.0013(16)	0.0066(15)	−0.0042(15)
$O_{term}3$	0.0087(19)	0.0172(18)	0.0182(17)	0.0070(16)	−0.0042(14)	0.0015(16)
$O_{term}4$	0.0148(19)	0.0093(18)	0.0171(18)	0.0040(14)	0.0068(15)	0.0012(14)
$O_{term}5$	0.0082(19)	0.0111(18)	0.0155(15)	0.0013(14)	−0.0032(13)	0.0025(13)
$O_{term}6$	0.012(18)	0.0126(17)	0.0075(16)	0.0000(14)	−0.0025(14)	−0.0054(15)
$O_{term}7$	0.0073(17)	0.0113(18)	0.0168(18)	−0.0026(14)	0.0054(14)	−0.0006(14)
O_H1	0.012(2)	0.0154(19)	0.0176(18)	−0.0077(15)	−0.0019(15)	−0.0002(14)

Table 8 Refined atomic coordinates, Wyckoff symbols and isotropic displacement parameters U_{eq}/Å^2 in Ho[H(PO$_3$)$_4$]

Atom	Wyckoff symbol	X	y	z	U_{eq}
Ho1	4e	0.729532(17)	0.05657(3)	0.05931(3)	0.00637(13)
P1	4e	0.90118(10)	−0.3250(2)	0.12488(15)	0.0080(3)
P2	4e	0.89935(9)	0.1530(2)	−0.18799(15)	0.0073(3)
P3	4e	0.38820(10)	0.2885(2)	0.20467(15)	0.0070(3)
P4	4e	0.59443(10)	0.3988(2)	0.21039(15)	0.0070(3)
$O_{br}1$	4e	0.9438(3)	−0.0209(6)	−0.2624(4)	0.0138(9)
$O_{br}2$	4e	0.9995(3)	−0.2308(5)	0.0942(4)	0.0101(8)
$O_{br}3$	4e	0.4186(3)	0.1212(5)	0.3132(4)	0.0111(8)
$O_{br}4$	4e	0.4853(3)	0.3257(6)	0.1412(4)	0.0107(8)
$O_{term}1$	4e	0.8334(3)	−0.1891(5)	0.1737(4)	0.0117(8)
$O_{term}2$	4e	0.8395(3)	0.0788(6)	−0.0889(5)	0.0166(9)
$O_{term}3$	4e	0.8581(3)	0.2080(6)	0.2034(4)	0.0154(9)
$O_{term}4$	4e	0.6349(3)	−0.0475(5)	0.2120(4)	0.0125(9)
$O_{term}5$	4e	0.6904(3)	−0.2267(6)	−0.0824(4)	0.0119(8)
$O_{term}6$	4e	0.6161(3)	0.1414(6)	−0.1351(4)	0.0132(9)
$O_{term}7$	4e	0.6633(3)	0.3331(5)	0.1200(4)	0.0121(9)
O_H1	4e	0.8568(3)	−0.4297(6)	−0.0126(5)	0.0178(10)
H1	4e	0.795(3)	−0.394(12)	−0.068(7)	0.050

Table 9 Anisotropic displacement parameters U_{ij}/Å^2 in Ho[H(PO$_3$)$_4$]

Atom	U_{11}	U_{22}	U_{33}	U_{12}	U_{13}	U_{23}
Ho1	0.00672(16)	0.00555(17)	0.00677(17)	−0.00023(10)	0.00109(10)	−0.00002(10)
P1	0.0072(6)	0.0059(7)	0.0103(7)	0.0007(6)	0.0004(6)	−0.0001(6)
P2	0.0053(6)	0.0069(7)	0.0094(7)	−0.0003(6)	0.0008(5)	−0.0011(6)
P3	0.0066(6)	0.0054 (7)	0.0088(7)	−0.0006(6)	0.0010(5)	−0.0006(5)
P4	0.0069(6)	0.0048(7)	0.0090(7)	−0.0015(6)	0.0002(6)	0.0001(5)
$O_{br}1$	0.0094(19)	0.012(2)	0.019(2)	−0.0050(18)	−0.0009(17)	0.0009(17)
$O_{br}2$	0.0121(19)	0.011(2)	0.0064(18)	0.0006(17)	0.0004(15)	−0.0025(16)
$O_{br}3$	0.018(2)	0.0037(19)	0.010(2)	0.0033(17)	0.0002(17)	−0.0011(17)
$O_{br}4$	0.0084(18)	0.015(2)	0.0093(19)	−0.0018(17)	0.0029(15)	−0.0026(16)
$O_{term}1$	0.0139(19)	0.010(2)	0.011(2)	0.0014(17)	0.0020(16)	0.0033(16)
$O_{term}2$	0.014(2)	0.019 (2)	0.018(2)	0.0005(19)	0.0064(18)	−0.0033(17)
$O_{term}3$	0.0119(19)	0.014(2)	0.018(2)	−0.0014(19)	−0.0037(17)	−0.0012(17)
$O_{term}4$	0.014(2)	0.010(2)	0.016(2)	0.0020(17)	0.0069(17)	−0.0008(16)
$O_{term}5$	0.0091(18)	0.010(2)	0.0015(2)	0.0004(18)	−0.0015(16)	0.0002(16)
$O_{term}6$	0.016(2)	0.010(2)	0.013(2)	−0.0019(17)	0.0000(17)	0.0043(17)
$O_{term}7$	0.0105(18)	0.010(2)	0.018(2)	−0.0016(18)	0.0068(17)	0.0006(16)
O_H1	0.015(2)	0.018(2)	0.017(2)	−0.0100(19)	−0.0039(18)	0.0004(17)

Table 10 Selected interatomic distances/pm and angles/°

	Tb[H(PO$_3$)$_4$]	Dy[H(PO$_3$)$_4$]	Ho[H(PO$_3$)$_4$]
Ln–O	228.0(3)–245.1(3)	224(2)–247(2)	2.254(4)–2.427(4)
P–O_{br}	156.1(3)–161.1(3)	145(3)–188(3)	1.568(4)–1.601(4)
P–O_{term}	146.2(3)–149.4(3)	130(2)–160(3)	1.463(4)–1.495(4)
P–O_H	153.3(3)	171 (3)	1.533(4)
P_{OH}–O_{br}–P_O	135.8(2)–135.90(2)	126.5(18)–134.9(16)	135.8(2)–136.3(3)
P_O–O_{br}–P_O	129.9(2)–132.5(2)	129.5(19)–141.5(19)	129.8(3)–132.6(3)
O_{term}–P–O_{term}	117.4(2)–121.4(2)	111(2)–118(3)	117.4(2)–121.2(2)
O_{term}–P–O_{br}	105.9(2)–114.3(2)	94(2)–130(3)	105.9(2)–114.1(2)
O_{term}–P–O_H	115.1(2)	135(2)	115.0(2)
O_{br}–P–O_{br}	99.4(2)–104.1(2)	93(2)–111(2)	99.1(2)–104.2(2)
O_{br}–P–O_H	104.6(2)–106.9(2)	98.1(20)–108.9(20)	104.7(2)–106.7(2)

Table 11 Rietveld refinement parameters of Dy[H(PO$_3$)$_4$]

Molar weight/g mol^{-1}	479.40
Crystal system	Monoclinic
Space group	$P2_1/c$ (no. 14)
Colour	Colourless
a/pm	1365.85(3)
b/pm	709.74(1)
c/pm	962.15(2)
β/°	101.116(1)
Volume/10^6 pm^3	915.21(3)
Z	4
Calculated density D_x/g cm^{-3}	3.479
Radiation	Cu-K_α
Wavelength λ/Å	1.5406
Diffractometer	Bruker D8 Advance
Theta range/°	$5.00 \leq 2\theta \leq 140.00$
Refined parameters	62
R_p	0.009
R_{wp}	0.012
χ^2	4.04

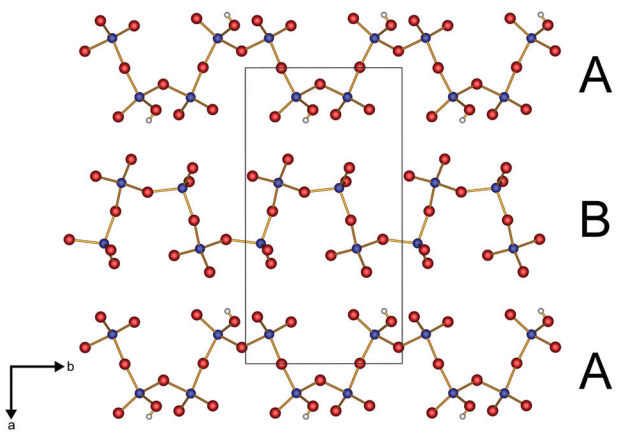

Fig. 1 Infinite, parallel hydrogen polyphosphate (A) and polyphosphate (B) chains of Ln[H(PO$_3$)$_4$] (Ln = Tb, Dy, Ho) along [010] (viewed along direction [001]); phosphorus blue, oxygen red, hydrogen white.

and 133°, respectively. Selected bond lengths and angles of Ln[H(PO$_3$)$_4$] (Ln = Tb, Ho) are listed in Table 10.

An appropriate method for the calculation of the deviation of tetrahedra from ideal symmetry was introduced by Balić-Žunić and Makovicky.[24,25] We adopted and explained the application of this method with the example of α-BaHPO$_4$;[26] in the course of our recent results we assigned deviations of less than 1% to regular tetrahedra. The four crystallographically

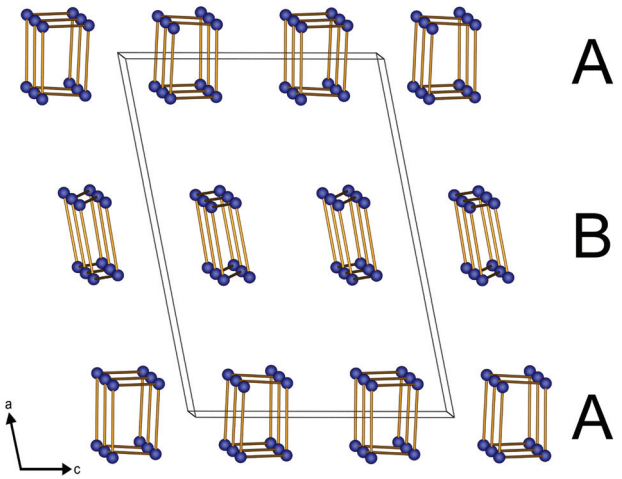

Fig. 2 Reduced presentation of the infinite helical poly-hydrogenphosphate (A) and polyphosphate (B) chains of $Ln[H(PO_3)_4]$ (Ln = Tb, Dy, Ho) viewing in the [010] direction. O and H atoms are omitted for clarity; phosphorus blue.

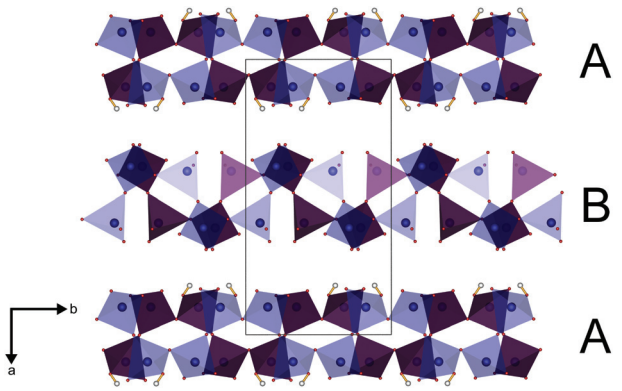

Fig. 3 Phase-shifted chains of poly-hydrogenphosphate (A) and polyphosphate (B) tetrahedra (blue: front, violet: back) of $Ln[H(PO_3)_4]$ (Ln = Tb, Dy, Ho) in [001]; phosphate tetrahedra blue, oxygen red, hydrogen white.

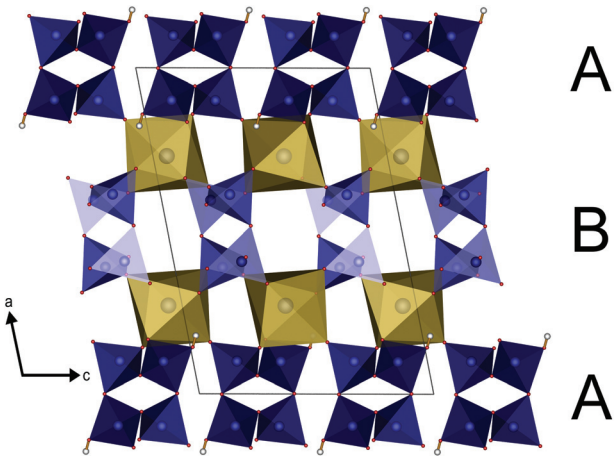

Fig. 4 Infinite helical chains of poly-hydrogenphosphate (A) and polyphosphate (B) tetrahedra in $Ln[H(PO_3)_4]$ (Ln = Tb, Dy, Ho) in the [010] direction interconnected *via* LnO_7 polyhedra (yellow); phosphate tetrahedra blue, oxygen red, hydrogen white.

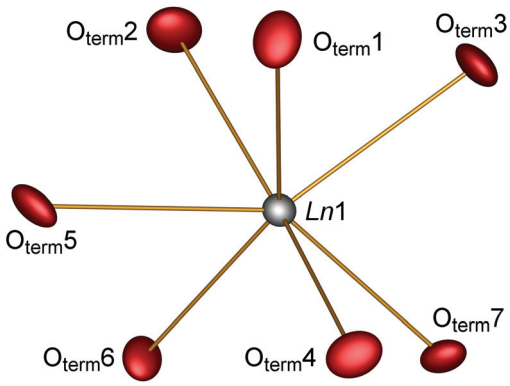

Fig. 5 Coordination sphere of the lanthanide in $Ln[H(PO_3)_4]$ (Ln = Tb, Dy, Ho). The displacement ellipsoids are drawn on a probability level of 70%.

different phosphate and hydrogenphosphate tetrahedra in $Tb[H(PO_3)_4]$ and $Ho[H(PO_3)_4]$ show the values of −0.32% (P1), −0.29 (P2), −0.22 (P3), −0.20 (P4) and −0.32 (P1), −0.29% (P2), −0.21 (P3), −0.21 (P4), respectively. These values are on the typical scale for phosphate tetrahedra.[22,26–29] Exhibiting a deviation far below 1%, all tetrahedra are classified as regular.

The parallel poly-hydrogenphosphate and polyphosphate chains of $Ln[H(PO_3)_4]$ (Ln = Tb, Dy, Ho) are interconnected *via* common O corners of LnO_7 polyhedra (Fig. 4). The single-crystal structure reveals a single site of Ln^{3+}, which is coordinated capped trigonal prismatic by seven terminal oxygen atoms of the polyphosphate chains (Fig. 5 and 6). The Ln–O bond lengths range between 225 and 245 pm (Table 10). These values are in the same range as the Er–O bond lengths in $Er[H(PO_3)_4]$ determined by Palkina *et al.*[17]

In $Ln[H(PO_3)_4]$ (Ln = Tb, Ho) a single hydrogen bond was found which can be considered as moderate according to

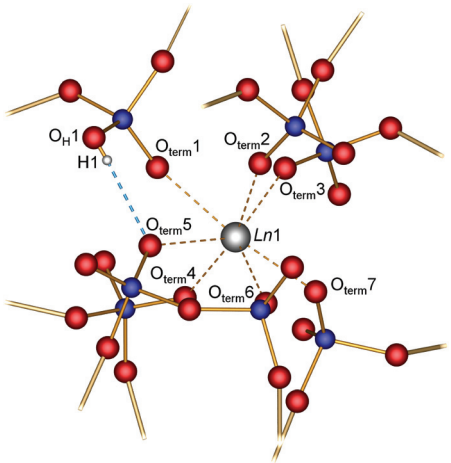

Fig. 6 Moderate hydrogen bond (dotted blue line) and coordination sphere of the Ln atom in $Ln[H(PO_3)_4]$ (Ln = Tb, Dy, Ho); phosphorus blue, oxygen red, hydrogen white.

Steiner.[30] $Tb[H(PO_3)_4]$ exhibits a hydrogen to acceptor distance d(H1–$O_{term}5$) of 176 pm and a bond angle ∢(DHA) of 165° (the donor to hydrogen distance $d(O_H1–H1)$ = 93 pm, and the donor to acceptor distance $d(O_H1–O_{term}5)$ = 267 pm). In $Ho[H(PO_3)_4]$ the hydrogen to acceptor distance d(H1–$O_{term}5$) is 185 pm and the bond angle ∢(DHA) is 145° (the donor to hydrogen distance $d(O_H1–H1)$ = 94 pm, and the donor to acceptor distance $d(O_H1–O_{term}5)$ = 266 pm) (Fig. 6). In contrast to moderate hydrogen bonds with a hydrogen to acceptor distance between 150 and 220 pm and bond angles ∢(DHA) larger than 130°, strong hydrogen bonds exhibit a distance of 120–150 pm and an angle of 170–180°.

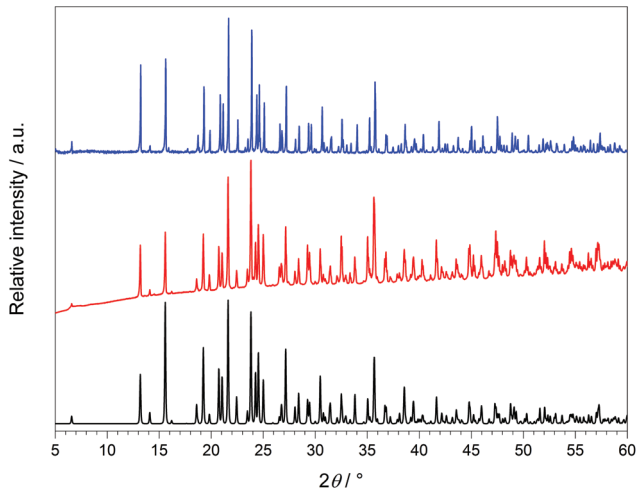

Fig. 7 X-ray powder diffraction patterns of $Tb[H(PO_3)_4]$ (red) and $Ho[H(PO_3)_4]$ (blue) and the calculated X-ray powder diffraction pattern from single-crystal data of $Tb[H(PO_3)_4]$ (black) ($\lambda_{Cu\text{-}K\alpha}$ = 1.54178 Å).

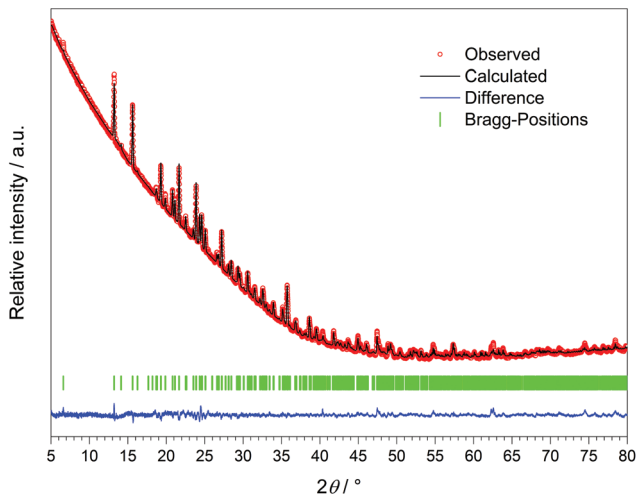

Fig. 8 X-ray powder diffraction pattern and the result of the Rietveld refinement of $Dy[H(PO_3)_4]$ ($\lambda_{Cu\text{-}K\alpha}$ = 1.54178 Å).

The crystal structure of $Dy[H(PO_3)_4]$ was refined *via* the Rietveld method (Fig. 8 and Table 11) based on the structure model of $Tb[H(PO_3)_4]$.

3 Electrostatic calculations

The coordination numbers of the lanthanide ions and the electrostatic consistency of the structure model were confirmed by calculations based on the MAPLE concept (Madelung Part of Lattice Energy).[31–33] The presence of one proton could also be proven. A structure model is electrostatically consistent if the sum of MAPLE values of chemically similar compounds deviates from the MAPLE value of the compound of interest by less than approximately 1%. Thus the structure models of $Tb[H(PO_3)_4]$ and $Ho[H(PO_3)_4]$ show electrostatic consistency (Table 1).

4 Infrared spectroscopy

The infrared spectra of $Ln[H(PO_3)_4]$ (Ln = Tb, Dy, Ho) were recorded between 4000 and 400 cm^{-1} and are shown in Fig. 9.

The bands between 1350 and 1200 cm^{-1} can be assigned to the asymmetric stretching vibrations of PO_2, while vibrations between 1200 and 990 cm^{-1} can be assigned to the stretching vibrations of PO_{term}. The $\nu_{as}(PO_{br})$ and ν_{as}(POP) vibrational bands range between 985 and 845 cm^{-1}.[11,36–38] The four symmetric stretching modes of the PO_{br} vibrations are detected between 780 and 650 cm^{-1} peaking at 681, 700, 741 and 770 cm^{-1}, which had been empirically correlated with the periodicity of polyphosphate chains in *catena*-polyphosphates.[11,36,39] This also holds for $Ln[H(PO_3)_4]$ (Ln = Tb, Dy, Ho), due to the periodicity P = 4 of its poly-hydrogenphosphate chains. Vibrations observed below 620 cm^{-1} are assigned to the bending vibrations of the PO_4 tetrahedra.[11,36–38] Surpris-

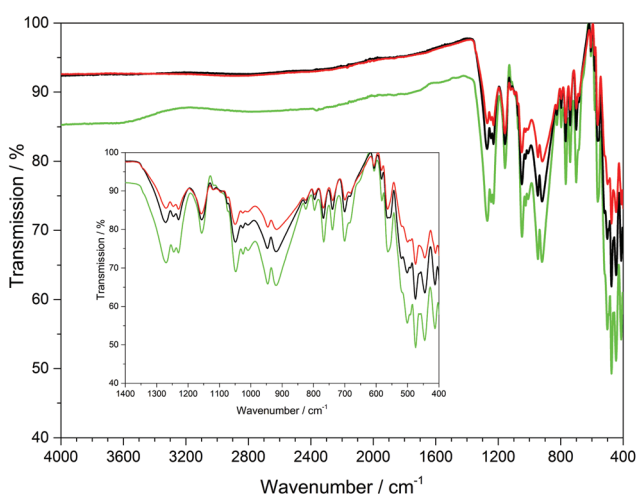

Fig. 9 Infrared spectra of $Ln[H(PO_3)_4]$ (Ln = Tb, Dy, Ho); terbium green, dysprosium black, holmium red.

ingly, no vibrations of the hydroxyl groups were detected, which leads to the assumption that presumably the ratio of O–H/P–O vibrations of 1 : 16 is too small to be detected *via* ATR.

5 UV/Vis spectroscopy

The UV/Vis reflection spectra of $Ln[H(PO_3)_4]$ (Ln = Tb, Dy, Ho) (Fig. 10–12) reveal the typical absorption bands of the f–f transitions of Tb^{3+}, Dy^{3+} and Ho^{3+} ions, according to the well-known energy level schemes.[40,41] All transitions start from the respective ground states $^7F_6$, $^6H_{15/2}$ and $^5I_8$ with the electronic configuration [Xe] $4f^8$, [Xe] $4f^9$ and [Xe] $4f^{10}$, respectively. The corresponding assignments are listed in Tables 2–4.

No significant deviations from the spectra of other inorganic salts of terbium, dysprosium and holmium were detected and the spectra are in accordance with the powder colours white ($Tb[H(PO_3)_4]$ and $Dy[H(PO_3)_4]$) and pink/yellow ($Ho[H(PO_3)_4]$). Like other holmium compounds $Ho[H(PO_3)_4]$ shows the alexandrite effect.[43,44] Due to an absorption gap in the yellow region, it exhibits a yellow body colour in ambient day light. In artificial light, *e.g.* fluorescent lamps, exhibiting distinct emissions in the blue (~450 nm), green (~540 nm) and red (~610 nm) range, it reveals a pink body colour, due to the reflection of the wavelengths between 550 and 620 nm.[4]

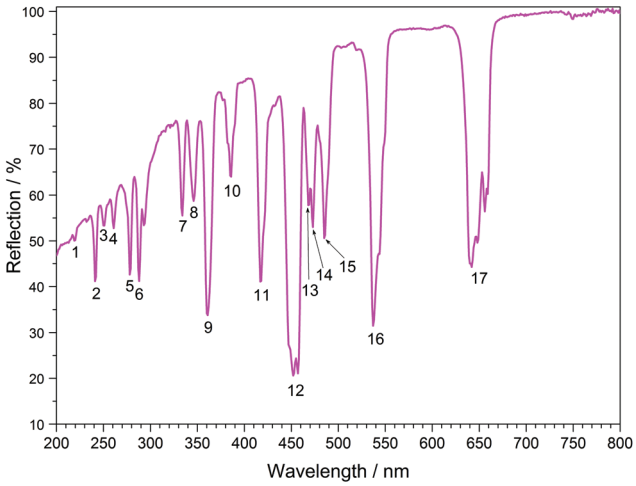

Fig. 12 UV/Vis spectrum of $Ho[H(PO_3)_4]$.

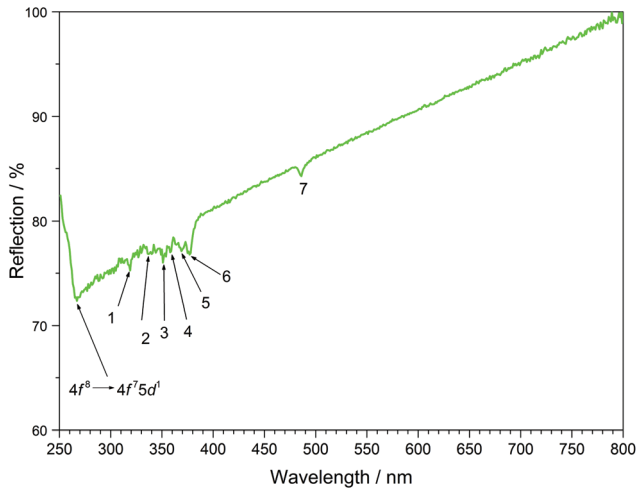

Fig. 10 UV/Vis spectrum of $Tb[H(PO_3)_4]$.

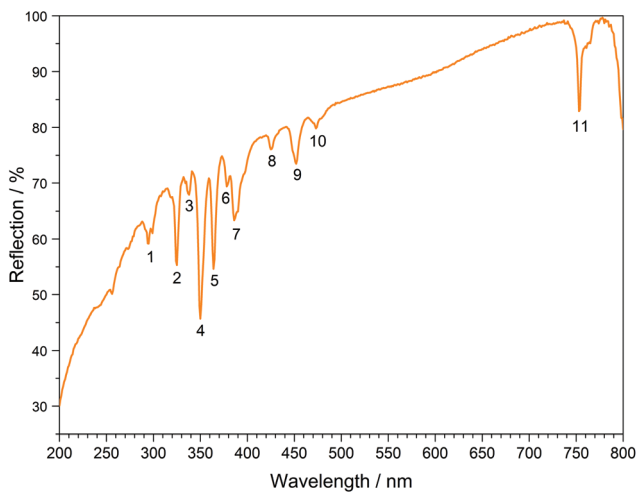

Fig. 11 UV/Vis spectrum of $Dy[H(PO_3)_4]$.

6 Fluorescence spectroscopy

The fluorescence spectra of $Tb[H(PO_3)_4]$ (Fig. 13) and $Dy[H(PO_3)_4]$ (Fig. 14) reveal the characteristic f–f emissions of Tb^{3+} and Dy^{3+}, respectively.[40–42]

Between 230 and 267 nm a broader band in the excitation spectrum of $Tb[H(PO_3)_4]$ reveals the parity allowed $4f^8 \rightarrow$

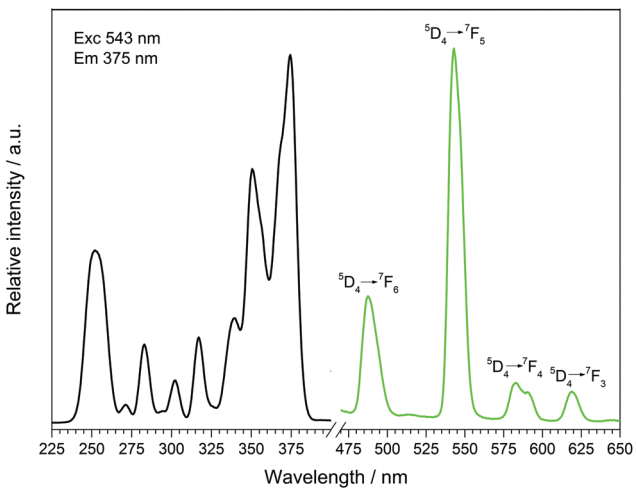

Fig. 13 Excitation (black), recorded at λ_{Em} = 543 nm, and emission (green) spectrum, recorded at λ_{Exc} = 375 nm, of $Tb[H(PO_3)_4]$.

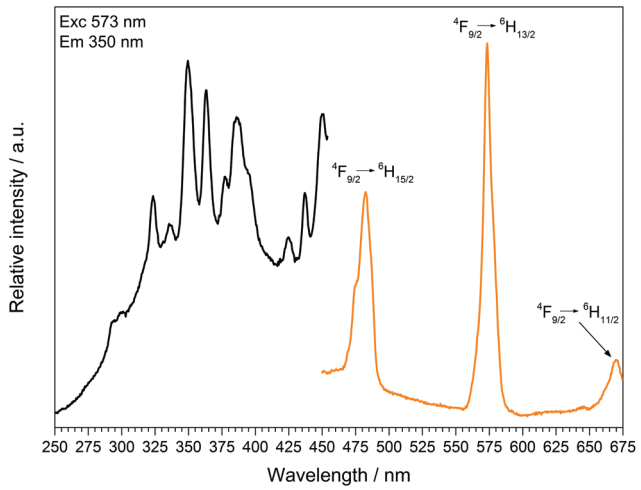

Fig. 14 Excitation (black), recorded at λ_{Em} = 573 nm, and emission (orange) spectrum, recorded at λ_{Exc} = 350 nm, of $Dy[H(PO_3)_4]$.

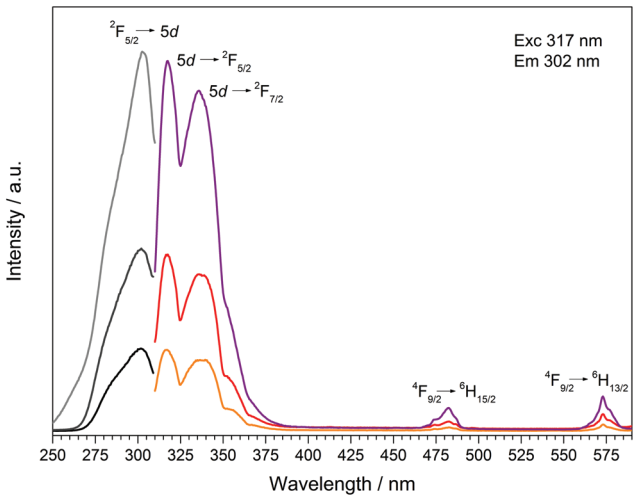

Fig. 15 Excitation, recorded at λ_{Em} = 317 nm, and emission spectra, recorded at λ_{Exc} = 302 nm, of $Dy[H(PO_3)_4]:Ce^{3+}$(5% black/orange, 10% dark grey/red, 30% grey/violet).

$4f^7 5d^1$ transition. Under excitation at 375 nm $Tb[H(PO_3)_4]$ exhibits sharp emission lines between 475 and 630 nm, which can be assigned to the $^5D_4 \rightarrow {}^7F_6$ (488 nm), $^5D_4 \rightarrow {}^7F_5$ (543 nm) showing the highest intensity, $^5D_4$ row $^7F_4$ (583 nm) and $^5D_4 \rightarrow {}^7F_3$ (619 nm) transitions.[42]

The excitation spectrum of $Dy[H(PO_3)_4]$ exhibits a broad band around 290 nm, which reveals the $4f^9 \rightarrow 4f^8 5d^1$ transition. Under excitation at 349 nm $Dy[H(PO_3)_4]$ exhibits sharp emission lines between 460 and 675 nm, which correspond to the f–f electronic transitions $^4F_{9/2} \rightarrow {}^6H_{15/2}$ (482 nm), $^4F_{9/2} \rightarrow {}^6H_{13/2}$ (573 nm) and $^4F_{9/2} \rightarrow {}^6H_{11/2}$ (671 nm).[41] The most intense transition $^4F_{9/2} \rightarrow {}^6H_{13/2}$ is sensitive to the surrounding of Dy^{3+}, and is thus called hypersensitive. The surrounding of Dy^{3+} in $Dy[H(PO_3)_4]$ is of relatively low symmetry (single capped trigonal prismatic), therefore the intensity of the hypersensitive transition is increased with respect to the $^4F_{9/2} \rightarrow {}^6H_{15/2}$ transition.[45,46]

Doping of $Dy[H(PO_3)_4]$ with increasing concentrations of Ce^{3+} (5, 10, 30 mol%) was carried out to investigate the effect of Ce^{3+} as a sensitizer. The presence of cerium and the corresponding ratios of Dy : Ce were investigated *via* EDX spectroscopy. The resulting ratios are 1 : 0.04 (expected: 1 : 0.05), 1 : 0.07 (1 : 0.10) and 1 : 0.26 (1 : 0.30), which are within the limits of accuracy of the measurements very close to the expected values. Due to an overlap in the wavelength range of the emission bands of Ce^{3+} and the excitation spectrum of Dy^{3+} energy transfer could be expected. Transitions in Ce^{3+} are f–d transitions, which are allowed due to the selection rules, and thus lead to broad and intense bands in the fluorescence spectrum.[13] The fluorescence spectra of the doped samples $Dy[H(PO_3)_4]:Ce^{3+}$ are shown in Fig. 15. The excitation spectra exhibit strongly increasing broad band intensities of Ce^{3+} at 302 nm ($^2F_{5/2} \rightarrow$ 5d). In the emission spectra, next to the typical broad band emissions of Ce^{3+} peaking at 317 nm (5d $\rightarrow {}^2F_{5/2}$) and 336 nm (5d $\rightarrow {}^2F_{7/2}$)[47,48] two comparably weak emission bands of Dy^{3+}, corresponding to the f–f electronic transitions $^4F_{9/2} \rightarrow {}^6H_{15/2}$ and $^4F_{9/2} \rightarrow {}^6H_{13/2}$, can be observed. Despite the low Dy^{3+} emission intensities the hypersensitive transition $^4F_{9/2} \rightarrow {}^6H_{13/2}$ can still be observed with higher intensity compared to the $^4F_{9/2} \rightarrow {}^6H_{15/2}$ transition. Doubling the content of Ce^{3+} from 5 to 10% the emission intensity of Dy^{3+} also increases equally ($^4F_{9/2} \rightarrow {}^6H_{15/2}$), whereas the hypersensitive transition $^4F_{9/2} \rightarrow {}^6H_{13/2}$ even triples. A further increase of the Ce^{3+} content to 30% leads to a raised intensity of a factor of 2.5 for the $^4F_{9/2} \rightarrow {}^6H_{15/2}$ transition and a factor of 1.7 for the $^4F_{9/2} \rightarrow {}^6H_{13/2}$ transition. Thus the emission intensities of Dy^{3+} increase slightly with the increasing Ce^{3+} content but do not prove efficient $Ce^{3+} \rightarrow Dy^{3+}$ energy transfer. The intensity of the f–d transition in the excitation spectrum increases corresponding to the increasing Ce^{3+} content. According to Luo and Yang satisfying energy transfer rates in the system Dy^{3+}/Ce^{3+} could be reached, if the ratio of Dy^{3+} to Ce^{3+} ions is decreased to about 1 : 3, before the luminescence quenching of Ce^{3+} occurs.[49–51] By reversing the Dy^{3+}/Ce^{3+} ratio and increasing the content of Ce^{3+} to $Ce_{0.75}Dy_{0.25}[H(PO_3)_4]$ efficient energy transfer might be reached, which represents a substitution process rather than a doping process.

Doping $Dy[H(PO_3)_4]$ with 5 mol% Eu^{3+} leads to the typical sharp excitation and emission bands of Dy^{3+} and Eu^{3+} (Fig. 16). The ratio of Dy : Eu was investigated *via* EDX spectroscopy exhibiting a ratio of 1 : 0.04, which is very close to the expected ratio (1 : 0.05). Under excitation at 392 nm $Dy[H(PO_3)_4]:Eu^{3+}$ exhibits sharp emission lines between 530 and 757 nm, which can be assigned to the $^5D_1 \rightarrow {}^7F_1$ (536 nm), $^5D_0 \rightarrow {}^7F_0$ (553 nm), $^5D_0 \rightarrow {}^7F_1$ (593 nm), $^5D_0 \rightarrow {}^7F_2$ (614 nm), $^5D_0 \rightarrow {}^7F_3$ (646 nm), $^5D_1 \rightarrow {}^7F_5$ (663 nm), $^5D_0 \rightarrow {}^7F_4$ (700 nm) and $^5D_0 \rightarrow {}^7F_5$ (750 nm) transitions of Eu^{3+}.[52] The most intense transition $^5D_0 \rightarrow {}^7F_2$ at 614 nm is called hypersensitive due to its sensitivity to the surrounding of Eu^{3+} and is responsible for

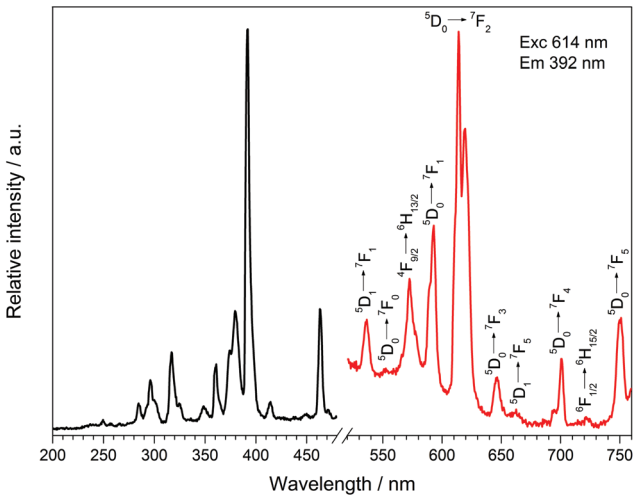

Fig. 16 Excitation (black), recorded at λ_{Em} = 614 nm, and emission (red) spectrum, recorded at λ_{Exc} = 392 nm, of $Dy[H(PO_3)_4]:Eu^{3+}$.

the weak red emission. It is dominant over the $^5D_0 \rightarrow {}^7F_1$ transition because of the asymmetric surrounding of Eu^{3+} in $Dy[H(PO_3)_4]:Eu^{3+}$, which proves its partial substitution of Dy^{3+}.[53,54] Besides the emission bands of Eu^{3+} two emission bands of Dy^{3+} can be observed at 573 and 722 nm, which can be assigned to the $^4F_{9/2} \rightarrow {}^6H_{13/2}$ and $^6F_{1/2} \rightarrow {}^6H_{15/2}$ transitions of Dy^{3+}, respectively.[41]

7 Magnetic properties

Due to the presence of one proton and the thus postulated sum formula of $Tb[H(PO_3)_4]$, the valence state of terbium was confirmed by the magnetic susceptibility measurement, which was recorded in a field of 1000 Oe over the temperature range of 1.8 K < T < 400 K (Fig. 17). In the whole temperature range the molar susceptibility obeys Curie's law ($\chi_m = C/T$) very well with a Curie constant of C = 11.3792 emu mol^{-1} K^{-1}. The Curie constant corresponds to an effective magnetic moment per Tb^{3+} ion of $\mu_{eff} = 9.54\mu_B$, which is close to the theoretical value ($\mu_{eff} = 9.72\mu_B$) and to experimental effective magnetic moments of Tb^{3+} ions (9.7–9.8μ_B).[55]

8 Thermal analysis

The thermal behaviour of $Tb[H(PO_3)_4]$ was investigated between room temperature and 1450 °C (Fig. 18). The thermogravimetric curve revealed several undefined steps with a total mass loss of 15.2 wt% in the temperature range of 500–1450 °C. Assuming that besides 0.5 moles of H_2O a further 0.5 moles of P_2O_5 evaporate (theor. mass loss: 16.8 wt%) a final composition of TbP_3O_9 may be assumed. After the thermal treatment the product was glazed and the expected composition could not be confirmed *via* X-ray powder diffraction.

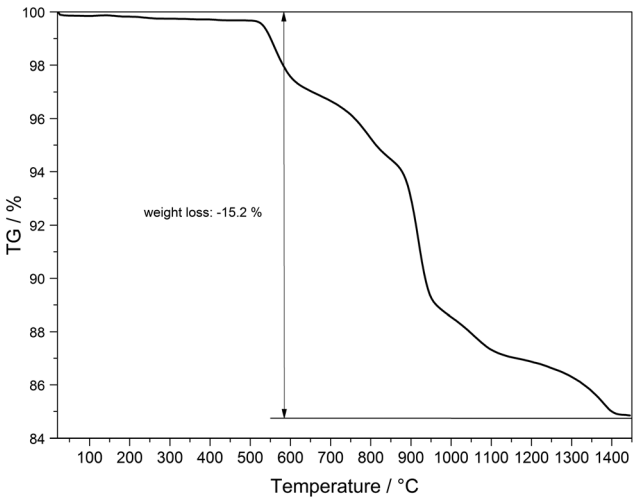

Fig. 18 Thermogravimetric analysis of $Tb[H(PO_3)_4]$.

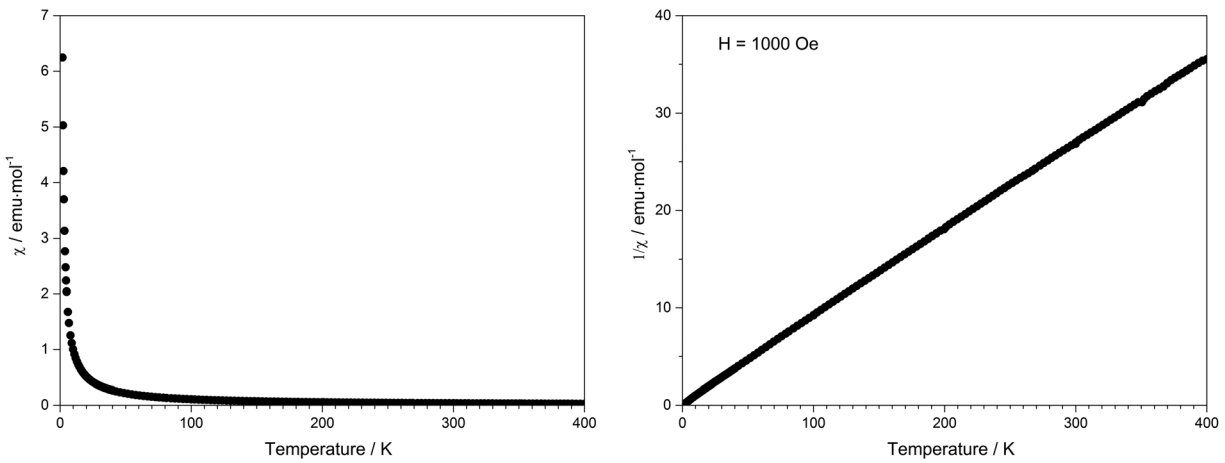

Fig. 17 Temperature dependence of the magnetic susceptibility χ of $Tb[H(PO_3)_4]$.

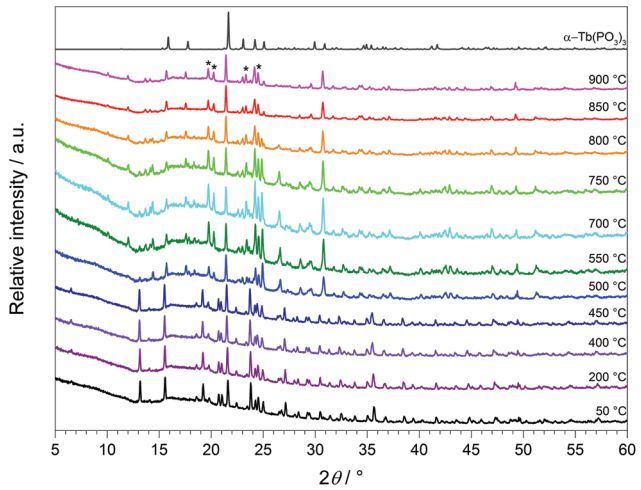

Fig. 19 Temperature-dependent X-ray powder diffraction patterns of $Tb[H(PO_3)_4]$ recorded between 50 and 900 °C and the calculated powder diffraction pattern from the single-crystal data of α-TbP_3O_9 (grey) ($\lambda_{Cu\text{-}K\alpha}$ = 1.54178 Å).

Temperature-dependent X-ray powder diffraction confirms that $Tb[H(PO_3)_4]$ is stable up to 500 °C (Fig. 19). At 900 °C α-TbP_3O_9 (grey) represents the main phase next to a small part of TbP_5O_{14} (marked with *).[56] This leads to the conclusion that the assumption of losing half a mole of each, H_2O and P_2O_5, in the thermal analysis is correct. $Tb[H(PO_3)_4]$ exhibits infinite chains of $[H(PO_3)_4]^{3-}$ and $[P_3O_9]^{3-}$ anions. Hence it is not surprising that thermal decomposition leads to the elimination of the hydroxyl groups by evaporation of water. Astonishingly, under nitrogen flow this process does not occur below 500 °C.

The thermal decomposition of $Ln[H(PO_3)_4]$ (Ln = Y, Gd–Er) was determined between 350 and 600 °C by Selevich *et al.*[57] According to the authors all investigations were carried out in atmospheric humidity. Thus thermal analysis was carried out in air and naturally proceeds in a shorter and lower temperature range (350–600 °C) rather than under an inert atmosphere (500–1440 °C) as performed in this work. Since an increasing stability is to be expected with an increasing connectivity, the thermal stability of $Tb[H(PO_3)_4]$, exhibiting infinite polyphosphate chains, is estimated to be higher than for non-condensed cyclotetraphosphates, *e.g.* $Ba_2(P_4O_12)\cdot3.5H_2O$,[27] which decomposes around 380 °C. In contrast, thermal decomposition of the ultraphosphate YP_5O_14, which reveals a higher degree of condensation, does not occur until 760 °C.[58]

9 Conclusions

In this contribution we demonstrated the crystal structures of $Ln[H(PO_3)_4]$ (Ln = Tb, Dy, Ho), which were solved and refined based on single-crystal X-ray diffraction (Tb and Ho) and refined by a Rietveld refinement (Dy), respectively. Via MAPLE calculations the presence of a single proton could be proved on the one hand, and on the other hand the electrostatic consistency of the structure model of $Ln[H(PO_3)_4]$ (Ln = Tb, Ho) was confirmed. All the observed bands in the IR spectrum are in agreement with our structure model. The optical properties reveal the typical UV/Vis reflection and fluorescence spectra of Tb^{3+}, Dy^{3+} and Ho^{3+} ions exhibiting their characteristic absorption and emission bands. Doping of $Dy[H(PO_3)_4]$ with increasing amounts of Ce^{3+} revealed only slightly more intense emission bands of Dy^{3+} in the blue and yellow regions. Doping of $Dy[H(PO_3)_4]$ with Eu^{3+} leads to a partial occupancy of Dy^{3+} sites, which is in accordance with the relatively high intensity of the hypersensitive $^5D_0 \rightarrow {}^7F_2$ transition of Eu^{3+} in a non-centrosymmetric surrounding. The magnetic measurements reveal no interaction between the Tb^{3+} centres and confirmed the oxidation state of Tb^{3+} and thus the composition of $Tb[H(PO_3)_4]$. Though $Tb[H(PO_3)_4]$ only reveals a condensation in one dimension, it exhibits a remarkable thermal stability up to 500 °C before presumably H_2O and P_2O_5 are released.

10 Experimental section

10.1 Syntheses of $Ln[H(PO_3)_4]$ (Ln = Tb, Dy)

$Ln[H(PO_3)_4]$ (Ln = Tb, Dy) were synthesised *via* solid-state reactions starting from the respective lanthanide oxides and phosphorous acid. Tb_4O_7 (94.70 mg, 0.14 mmol, Chempur, 99.9%) and Dy_2O_3 (94.00 mg, 0.25 mmol, Kristallhandel Kelpin, 99.99%), respectively, and H_3PO_3 (264.10 mg, 3.22 mmol, Sigma Aldrich, 99%) were ground in an agate mortar and transferred into a silica glass crucible. The reaction mixtures were covered with H_2O_2 (20 ml, Merck, 30%) to suppress the formation of LnP_3O_9 (Ln = Tb, Dy) as the side phase and heated up to 380 °C with a heating rate of 100 °C/h using a muffle furnace. The temperature was maintained for three hours before cooling down to room temperature by switching off the furnace. The products were washed with hot water and dried in air overnight. Different experiments showed that addition of H_2O_2 to the reaction mixtures leads to phase pure samples of colourless $Tb[H(PO_3)_4]$ and $Dy[H(PO_3)_4]$.

10.2 Synthesis of $Ho[H(PO_3)_4]$

$Ho[H(PO_3)_4]$ was synthesised analogously to $Ln[H(PO_3)_4]$ (Ln = Tb, Dy) but could be obtained as phase pure yellow/pink powder without addition of H_2O_2 to the reaction mixture.

10.3 X-Ray powder diffraction

The crystalline sample was finely ground, enclosed in a Hilgenberg glass capillary of 0.3 mm outer diameter and investigated at room temperature with a Bruker D8 Advance diffractometer using Cu-K_α radiation (LynxEye 1-D detector, steps of 0.2°, acquisition time 7 s per step, Soller slits 2.5°, fixed divergence slit 8 mm, transmission geometry). The obtained products were phase pure according to X-ray powder diffractometry (Fig. 7). The structure models of $Tb[H(PO_3)_4]$ and $Ho[H(PO_3)_4]$ were confirmed and the structure model of $Dy[H(PO_3)_4]$ was refined by Rietveld analysis[59,60] (Fig. 8) using the FullProf program suite and the WinPlotR graphical user interface.[61]

The single-crystal data of $Tb[H(PO_3)_4]$ served as the starting structure model. The structure of $Dy[H(PO_3)_4]$ was refined to excellent residuals of R_p = 0.009, R_{wp} = 0.012 and χ^2 = 4.04 (Table 11). The phase purity of $Dy[H(PO_3)_4]$ could thus be confirmed. In Table 11 the data of the Rietveld refinement of $Dy[H(PO_3)_4]$ are summarised.

The composition of $Ln[H(PO_3)_4]$ (Ln = Tb, Dy, Ho) was checked *via* EDX (Energy-dispersive X-ray) spectroscopy. For the doped samples $Dy[H(PO_3)_4]$:Ce and $Dy[H(PO_3)_4]$:Eu the ratios of Dy : Ce and Dy : Eu were also confirmed. Within the accuracy of the measurement limits no other elements were found.

10.4 Crystal structure determination of $Ln[H(PO_3)_4]$(Ln = Tb, Ho)

Single-crystals suitable for single-crystal X-ray diffraction analysis were selected under a polarizing microscope. Diffraction data were collected with a Bruker D8 Venture diffractometer using Mo-K_α radiation (λ = 0.7093 Å) at a temperature of 293 ± 2 (Ln = Tb) and 296 ± 2 K (Ln = Ho), respectively.

The structure of the non-merohedrally twinned crystal of $Tb[H(PO_3)_4]$ was solved by defining the twinned components using TWINABS (twin matrix: 0 0 1 0 −1 0 1 0 0; BASF = 0.430).[62] Both crystal structures were solved by direct methods and refined by the full-matrix least-squares technique with the SHELXTL crystallographic software package.[63,64] The Tb/Ho, P and O atoms could be clearly located. The hydrogen atom was added geometrically and was confirmed by MAPLE calculations.[31–33] Relevant crystallographic data and further details of the structure determination are summarised in Table 5. Tables 6–9 show the atomic coordinates and displacement parameters.

Further details of the crystal structure investigations presented in this work may be obtained from the Fachinformationszentrum Karlsruhe, D-76344 Eggenstein-Leopoldshafen, Germany (Fax: +49-7247-808-666; E-mail: crysdata@fiz-karlsruhe.de, http://www.fiz-karlsruhe.de/request for deposited data.html) on quoting the depository numbers CSD 429861 ($Tb[H(PO_3)_4]$) and CSD 429860 ($Ho[H(PO_3)_4]$).

10.5 Infrared spectroscopy

Infrared spectra were recorded at room temperature with a Bruker Equinox 55 FT-IR spectrometer using a Platinum ATR device with a scanning range from 4000 to 400 cm^{-1}.

10.6 UV/Vis spectroscopy

The optical reflection spectra were recorded with a Varian Cary 300 Scan UV/Vis spectrophotometer in the range of 200–800 nm.

10.7 Fluorescence spectroscopy

Excitation and emission spectra were recorded at room temperature with a Fluoromax-4 spectrofluorometer with a Xe plasma lamp (Horiba Scientific, Unterhaching).

10.8 Magnetic investigations

The temperature-dependent magnetic susceptibility data were recorded with a Quantum Design MPMS-XL super-conducting quantum-interference device (SQUID) magnetometer in the field of 1000 Oe between 1.8 K < T < 400 K.

10.9 Thermal analysis

The thermal analysis was carried out with a Netzsch STA-409 PC thermal analyzer in the temperature range of 25–1450 °C in air with a heating rate of 5 K min^{-1}.

Acknowledgements

The authors thank Dana Vieweg, Lehrstuhl für Experimentalphysik V, Universität Augsburg, for recording the magnetic susceptibility measurements and Dr Stefan Riegg, Lehrstuhl für Experimentalphysik V, Universität Augsburg, for valuable discussions about the magnetic measurement and the Rietveld refinement.

References

1 A. Holleman and E. Wiberg, *Lehrbuch der Anorganischen Chemie*, deGruyter, Berlin, New York, 102nd edn, 2007.
2 A. Durif, *Crystal Chemistry of Condensed Phosphates*, Plenum Press, New York, 1995.
3 C. Feldmann, T. Jüstel, C. Ronda and P. Schmidt, *Adv. Funct. Mater.*, 2003, **13**, 511–516.
4 T. Jüstel, H. Nikol and C. Ronda, *Angew. Chem., Int. Ed.*, 1998, **37**, 3084–3103.
5 T. Jüstel, C. Feldmann and C. R. Ronda, *Phys. Biol.*, 2000, **56**, 55–58.
6 T. Jüstel, J.-C. Krupa and D. U. Wiechert, *J. Lumin.*, 2001, **93**, 179–189.
7 C. R. Ronda, T. Jüstel and H. Nikol, *J. Alloys Compd.*, 1998, **275–277**, 669–676.
8 H. A. Höppe, K. Kazmierczak, S. Kacprzak, I. Schellenberg and R. Pöttgen, *Dalton Trans.*, 2011, **40**, 9971–9976.
9 H. A. Höppe, M. Daub and M. C. Bröhmer, *Chem. Mater.*, 2007, **19**, 6358–6362.
10 H. A. Höppe, *Angew. Chem., Int. Ed.*, 2009, **48**, 3572–3582.
11 H. A. Höppe and J. M. U. Panzer, *Eur. J. Inorg. Chem.*, 2009, 3127–3130.
12 G. H. Dieke and H. M. Crosswhite, *Appl. Opt.*, 1963, **2**, 675–686.
13 K. Ogasawara, S. Watanabe, H. Toyoshima and M. G. Brik, *Handbook on the Physics and Chemistry of Rare Earths*, Elsevier, 2007, vol. 37.
14 L. Ozawa, *Chem. Rev.*, 2003, **103**, 3835–3855.
15 K. Palkina and K. H. Jost, *Acta Crystallogr., Sect. B: Struct. Crystallogr. Cryst. Chem.*, 1975, **31**, 2285–2290.
16 K. Palkina, N. Kuzmina, A. Selevich and A. Lesnikovich, *Russ. J. Inorg. Chem.*, 2003, **48**, 161–164.
17 K. Palkina, N. Chudinova and G. Balagina, *Izves. Akad. Nauk SSSR*, 1982, **18**, 1337–1341.
18 K. H. Jost, *Z. Kristallogr.*, 1963, **16**, 623–626.
19 M. Rzaigui and K. Arigiub, *J. Solid State Chem.*, 1983, **50**, 240–246.

20 M. Graia, A. Driss and T. Jouini, *Solid State Sci.*, 2003, **5**, 393–402.
21 H. A. Höppe, *Solid State Sci.*, 2005, **7**, 1209–1215.
22 H. A. Höppe, *J. Solid State Chem.*, 2009, **182**, 1786–1791.
23 S. J. Sedlmaier and W. Schnick, *Z. Anorg. Allg. Chem.*, 2008, **634**, 1501–1505.
24 T. Balić-Žunić and E. Makovicky, *Acta Crystallogr., Sect. B: Struct. Sci.*, 1996, **52**, 78–81.
25 E. Makovicky and T. Balić-Žunić, *Acta Crystallogr., Sect. B: Struct. Sci.*, 1998, **54**, 766–773.
26 H. A. Höppe, M. Daub and O. Oeckler, *Solid State Sci.*, 2009, **11**, 1484–1488.
27 H. A. Höppe, K. Kazmierczak and M. Daub, *Z. Anorg. Allg. Chem.*, 2010, **636**, 1106–1110.
28 H. A. Höppe and M. Daub, *Z. Kristallogr.*, 2012, **227**, 535–539.
29 M. Daub, A. J. Lehner and H. A. Höppe, *Dalton Trans.*, 2012, **41**, 12121–12128.
30 T. Steiner, *Angew. Chem., Int. Ed.*, 2002, **41**, 48–76.
31 R. Hoppe, *Angew. Chem., Int. Ed. Engl.*, 1966, **5**, 95–106.
32 R. Hoppe, *Angew. Chem., Int. Ed. Engl.*, 1970, **9**, 25–34.
33 R. Hübenthal, *MAPLE, MAPLE, Program for the Calculation of the Madelung Part of Lattice Energy*, University of Gießen, Germany, 1993.
34 A. Goto, T. Hondoh and S. Mae, *J. Chem. Phys.*, 1990, **93**, 1412–1417.
35 C. H. MacGillavry, H. C. J. de Decker and L. M. Nijland, *Nature*, 1949, **164**, 448–449.
36 M. Weil, M. Puchberger, J. Schmedt auf der Günne and J. Weber, *Chem. Mater.*, 2007, **19**, 5067–5073.
37 J. Weidlein, U. Müller and K. Dehnicke, *Schwingungsfrequenzen I Hauptgruppenelemente*, Georg Thieme Verlag Stuttgart, New York, 1981.
38 A. Rulmont, R. Cahay, M. Liegeois-Duyckaerts and P. Tarte, *Eur. J. Solid State Inorg. Chem.*, 1991, **28**, 207–219.
39 O. Y. Miroshnichenko and V. V. Mombelli, *Russ. J. Inorg. Chem. Engl. Transl.*, 1979, **24**, 1631–1634.
40 W. T. Carnall, *J. Phys. Chem.*, 1963, **67**, 1206–1211.
41 W. T. Carnall, P. R. Fields and K. Rajnak, *J. Chem. Phys.*, 1968, **49**, 4424–4442.
42 W. T. Carnall, P. R. Fields and K. Rajnak, *J. Chem. Phys.*, 1968, **49**, 4447–4449.
43 H. A. Höppe, G. Kotzyba, R. Pöttgen and W. Schnick, *J. Mater. Chem.*, 2001, **11**, 3300–3306.
44 K. Kazmierczak and H. A. Höppe, *J. Solid State Chem.*, 2011, **184**, 1221–1226.
45 Y.-C. Li, Y.-H. Changa, Y.-F. Lin, Y.-S. Changb and Y.-J. Lin, *J. Alloys Compd.*, 2007, **439**, 367–375.
46 Z.-J. Zhang, J.-L. Yuan, H.-H. Chen, X.-X. Yang and J.-T. Zhao, *Solid State Sci.*, 2009, **11**, 549–555.
47 D. Bimberg, D. J. Robbins, D. R. Wight and J. P. Jeser, *Appl. Phys. Lett.*, 1975, **27**, 67–68.
48 M. Guan, J. Sun, T. Shang, Q. Zhou, J. Han and A. Ji, *J. Mater. Sci. Technol.*, 2010, **26**, 45–48.
49 C. Yang, Y. Pan and Q. Zhang, *Mater. Sci. Eng., B*, 2007, **137**, 195–199.
50 Q. Luo, X. Qiao, X. Fan, H. Yang, X. Zhang, S. Cui, L. Wang and G. Wang, *J. Appl. Phys.*, 2009, **105**, 043506.
51 H. Yu, W. Zi, S. Lan, S. Gan, H. Zou, X. Xu and G. Hong, *Luminescence*, 2013, **28**, 679–684.
52 W. T. Carnall, P. R. Fields and K. Rajnak, *J. Chem. Phys.*, 1968, **49**, 4450–4455.
53 G. Blasse, A. Bril and W. Nieuwpoort, *J. Phys. Chem. Solids*, 1966, **27**, 1587–1592.
54 G. Blasse and A. Bril, *J. Chem. Phys.*, 1967, **47**, 5442–5443.
55 H. Lueken, *Magnetochemie*, B. G. Teubner Stuttgart, Leipzig, 1999.
56 A. Durif, *Bull. Soc. Fr. Miner. Crystallogr.*, 1971, **94**, 314–318.
57 A. Selevich, A. Lyakhov and A. I. Lesnikovich, *Phosphorus Res. Bull.*, 1999, **10**, 171–176.
58 A. Mbarek, M. Graia, G. Chadeyron, D. Zambon, J. Bouaziz and M. Fourati, *J. Solid State Chem.*, 2009, **182**, 509–516.
59 H. M. Rietveld, *J. Appl. Crystallogr.*, 1969, **2**, 65–71.
60 H. M. Rietveld, *Z. Kristallogr.*, 2010, **225**, 545–547.
61 J. Rodríguez-Carvajal, *Phys. Rev. B: Condens. Matter*, 1993, **192**, 55–69.
62 G. M. Sheldrick, *TWINABS*, Universität Göttingen, 1996.
63 G. Sheldrick, *SHELXTL, Version 6.14*, Bruker AXS, 2003.
64 G. M. Sheldrick, *Acta Crystallogr., Sect. A: Fundam. Crystallogr.*, 2008, **64**, 112–122.